Ion tunnel matrix initiated oriented attachment for highly utilized Zn anodes

Dan Deng[1,#], Kai Fu[1,#], Ruohan Yu[1], Jiao Zhu[1], Hongwei Cai[1], Xiangchen Zhang[1], Jinsong Wu[1], Wen Luo[2,*] and Liqiang Mai[1,3,*]

[1]State Key Laboratory of Advanced Technology for Materials Synthesis and Processing, Wuhan University of Technology, Wuhan 430070, P. R. China

[2] Department of Physics, School of Science, Wuhan University of Technology, Wuhan 430070, P. R. China

[3] Hubei Longzhong Laboratory, Wuhan University of Technology (Xiangyang Demonstration Zone), Xiangyang 441000, China

#These authors contributed equally to this work.

E-mail: luowen_1991@whut.edu.cn; mlq518@whut.edu.cn

ABSTRACT

This article has been accepted for publication and undergone full peer review but has not been through the copyediting, typesetting, pagination and proofreading process, which may lead to differences between this version and the Version of Record. Please cite this article as doi: 10.1002/adma.202302353.

WILEY-VCH

Metallic zinc is an ideal anode for aqueous energy storage, however, Zn anodes suffer from nonhomogeneous deposition, low reversibility and dendrite formation; these lead to an over-provision of zinc metal in full cells. Herein, we report oriented-attachment-regulated Zn stacking initiated through a trapping-then-planting process with a high zinc utilization rate (ZUR). Due to the isometric topology features of cubic-type Prussian blue analogue (PBA), the initial Zn plating occurs at specific sites with equal spacing of ~5 Å in the direction perpendicular to the substrate; the trace amount of zinc ions trapped in tunnel matrix provides nuclei for the oriented attachment of Zn (002) deposits. As results, the PBA-decorated substrate delivers high reversibility of dendrite-free zinc plating/stripping for more than 6600 cycles (1320 h) and achieves an average Coulombic efficiency (CE) of 99.5% at 5 mA cm^{-2} with 100% ZUR. Moreover, the anode-limited full cell with a low negative-positive electrode ratio (N/P) of 1.2 can be operated stably for 360 cycles, displaying an energy density of 214 Wh kg^{-1}; this greatly exceeds commercial aqueous batteries. This work provides a proof-of-concept design of metal anodes with high utilization ratio and a practical method for developing high energy density batteries.

1. Introduction

Aqueous zinc metal batteries are one of the most promising alternatives to Li-ion batteries because of the inherent advantages of Zn anodes; these include intrinsic safety, high abundance, low electrochemical potential (-0.76 V *vs.* SHE), and high capacities (a gravimetric capacity of 820 mAh g^{-1} and a volumetric capacity of 5850 mAh cm^{-3}). Recently, several aqueous Zn-based energy storage devices, such as Zn-MnO_2[1], Zn-I_2[2] and Zn-air[3] batteries, have shown potential by exhibiting superior cycling stability and high theoretical energy density. In practice, however, Zn anodes must be used in a large excess under most conditions to maintain compensation during its consumption due to issues of corrosion, side reactions and isolated dendrites[4]. This nearly unlimited Zn reservoir (*i.e.*, Zn sheet or Zn foil) can potentially result in seemingly conspicuous cycling stability in laboratory tests but conceals the challenges caused by poor zinc reversibility in practical applications. The Zn utilization rate (ZUR, or depth of discharge) is a crucial but often disregarded metric for assessing how much of the hypothetical energy density can be utilized from an application perspective[4c, 5]. Therefore, it is thus highly desired to develop a facile strategy to achieve a reversible Zn anode with a high ZUR to potentially commercialize high energy density Zn-based batteries.

In general, a considerable portion of the Coulombic inefficiency of Zn plating/stripping comes from anisotropic deposition and the nonplanar morphology of deposited metallic Zn[6]. The randomly oriented structures lead to heterogeneous growth and dissolution, resulting in issues of dendrite formation and isolated Zn with a tendency to only partially dissolve during

subsequent cycles. Preferentially depositing Zn (002) crystal planes with a lower surface energy and higher atomic stacking density allows horizontal alignment of Zn crystallites, suppression of dendrite growth and restraint of side reactions[6b, 7]. To achieve regular (002) deposition and improve reversibility, various strategies have been employed, including electrolyte/solid interphase engineering[3b, 6d, 8], separator modification[6a, 7a, 9] and Zn/substrate surface design[10]. There are relatively few researches on the modification of zinc-free substrates, which is intrinsically suitable for application in high ZUR zinc anode applications (Table S1). In this regards, Zheng et al. reported a highly reversible (CE > 99.7% with 100% ZUR over 10000 cycles at 40 mA cm^{-2}) epitaxial aqueous Zn anode with locked (002) crystallographic orientation on a graphene substrate by exploiting the low lattice mismatch between substrate and metallic Zn[11]. Cui et al. demonstrated an anode-free Zn cell by constructing a carbon-based nucleation layer on Cu foil, which favours the reversibility of Zn to achieve a CE of 99.6% over 300 cycles[12]. A similar strategy was extended to an annealed ZIF-8-coated nickel grid, which provided homogeneous Zn deposition at 2 mA cm^{-2} and 1 mAh cm^{-2} to achieve an average CE of 98.6% over 200 cycles[13].

The zinc-free substrates reported thus far are relatively limited, and the application of Zn anodes with a high utilization rate remains an important research area. An ideal substrate should continuously regulate (002)-preferred Zn growth parallel to the electrode surface without interference from increased deposition thickness, depth of discharge (DOD) and cycle number. The early reported strategies for zinc-free substrate design, including introduction of low-lattice-mismatch interfaces[11, 14] or zincophillic layers[13, 15], have mostly

focused on modifying the two-dimensional (2D) plane of the substrate to regulate the epitaxial deposition of Zn. However, the electrodeposition of Zn on a substrate is a classic three-dimensional (3D) process. As electrodeposition proceeds, the distance between the substrate and the zinc deposition outer layer will become larger, and the regulation for Zn chemistry hardly retain after multiple cycles. Therefore, from this perspective, modulating the morphology evolution of Zn electrodeposition in a perpendicular-to-3D view with microscopic precision is the key to highly utilized Zn anodes (Fig. S1). In other words, to achieve horizontally arranged zinc platelet electrodeposits, the ideal deposition scheme is to regulate the initial nucleation of zinc atoms perpendicular to the substrate with an atomic spacing of ~4.94 Å, which matches the crystal plane spacing of Zn (002). Therefore, the introduction a zinc ion trap matrix on the substrate with the capability to fix zinc ions at equidistant intervals of ~4.94 Å perpendicular to the direction of the substrate would be beneficial.

Herein, we designed a proof-of-concept ion tunnel matrix consists of cubic-type Prussian blue analogue decorated carbon cloth (PBA@CC) substrate, in which a well-spaced PBA nanocubes function as zinc ion tunnel that assists highly reversible and Zn dendrite-free plating/stripping with high ZUR. In contrast to the previously reported PBA as host electrodes for various charge carrier ions, our study focuses on exploiting the potential of its highly regular, equally spaced cubic topology features. The distance between adjacent isometric cubic cages of the ZnFe-PBA framework is approximately 4.96 Å, which is very comparable to the crystal plane spacing of Zn (002). Therefore, the zinc ions trapped in the

nanocages of PBA spontaneously maintain an equally spaced arrangement of approximately 5 Å in the direction normal to the substrate and act as a zinc source in the initial deposition. This trapping-then-plating process facilitates the formation of low-lattice-mismatch interfaces, which is evidenced by spherical aberration electron microscope observation and ^{66}Zn isotope tracking technique. More importantly, even if metallic Zn is completely stripped at every cycle (100% ZUR), the PBA@CC shows highly reversible Zn plating/stripping at 5 mA cm^{-2} and 0.5 mAh cm^{-2} with 99.6% average CE up to 6,600 cycles (1320 h). The anode-limited full cell with a low negative-positive electrode ratio (N/P) of 1.2 delivers 214 Wh kg^{-1} and can be operated stably for 360 cycles. This work provides insight into rationally designed substrates for deeply rechargeable and highly reversible metal anodes.

2. Results and discussion

Horizontal Zn stacking initiated by oriented-attached deposition

The key issue of current Zn metal battery research is that thick Zn sheets have been overwhelmingly tested; these sheets show low ZURs (generally less than 5%) and have an imbalanced anode-cathode configuration (Fig. 1a). The nearly unlimited zinc reservoir potentially favours enhanced cycling stability in the laboratory but severely limits the actual energy density of full batteries. Simple calculations were performed to determine the influence of ZUR in assembling high-energy-density aqueous Zn metal batteries (Fig. 1b and Table S2). Pairing zinc sheet anodes of 5% ZUR with various cathodes, the specific energy densities of the listed Zn batteries are all below 55 Wh kg^{-1}; this is inferior to those of commercial aqueous systems such as Ni-MH, Ni-Cd and lead-acid batteries[16]. A higher

ZUR of 80% is needed to achieve specific energy densities in Zn metal batteries that are beyond commercial aqueous cells and to become competitive with Li-ion batteries.

In theory, Zn metal batteries with high ZUR can provide higher energy density but they need to exhibit a high overall CE and horizontally arranged electrodeposition on a Zn-limited or Zn-free substrate. In this regard, we aimed to achieve regular (002) deposition and improve reversibility of Zn anode, thereby the dendrites and low energy density problems could be solved. Fig. 1c exhibits schematic diagrams of the horizontal growth of Zn stacks induced by oriented attachment of the initial deposition lateral to a well-spaced ion tunnel matrix. Fig. 1c exhibits schematic diagrams of the horizontal growth of Zn stacks induced by oriented attachment of the initial deposition lateral to a well-spaced ion tunnel matrix. Before deposition, the matrix acts like a 'ladder' to automatically fix the zinc ions to the height of the trapping cage in the direction perpendicular to the substrate. Moreover, porous metal-organic frameworks (MOFs) are prospective adjustable platforms to find a serviceable ion trap and tunnel matrix via logical design. Given that the trace amount of zinc ions in the trap matrix works as nuclei, the initial Zn plating would occur at specific sites on the surface of MOF particles. Therefore, the MOF can be considered as an ideal zinc ion trap and tunnel matrix if its nanocavities are equally spaced at approximately 5 Å and exhibit a small lattice misfit with the (002) plane of metallic Zn. During Zn deposition, the as-deposited metal layer promotes homogeneous electrodeposition, locking the (002) crystallographic orientation on the substrate. The nucleus gradually grows and finally forms a horizontally arranged and aligned (002) galvanized layer that covers the substrate. The above trap-then-plant process

can in principle be repeated to achieve 100% ZUR; the deposited zinc is completely stripped in every cycle, since the exposed tunnel matrix can sustainably regulate zinc plating even with a Zn-free substrate during repeated cycles.

PBAs are archetypes of MOFs assembled from octahedrally coordinated cyanide bridging metal nodes with a 3D open structure (Fig. S2, Supporting Information). Since the cubic-type PBA framework is a matrix of ~5 Å isometric zinc ion traps and tunnels, we selected a cubic PBA crystal-decorated substrate (PBA@Ti or PBA@CC) for a proof-of-concept to demonstrate the above design strategy. In this study, we demonstrate that PBA nanocubes with high crystallinity, regular cubic morphology and narrow particle size distribution can be directly grown on a CC or Ti foil substrate via a moderate precipitation method by using potassium citrate as an inhibitor (see Fig. S3, and Experimental section, for details). All cubic-PBA@CC substrates (including ZnFe-PBA@CC, CuFe-PBA@CC and NiFe-PBA@CC) exhibit uniformly distributed PBA with clear cubic boundaries (Fig. S4-S5). In high-angle annular dark field (HAADF) scanning transmission electron microscopy (STEM) images, bright spots corresponding to metal nodes clearly show the characteristic square distribution representing the PBA framework (Fig. S6). X-ray diffraction (XRD) and Fourier transform infrared (FTIR) spectrometer confirm the single phase and crystallinity of the PBA cubes (Fig. S7-S8). Prior to plating/stripping tests, the PBAs rooted on the substrate underwent low-rate galvanostatic depotassium and zinc ion insertion procedures. This pre treatment was realized by simple electrochemical treatment by low-rate galvanostatic charging-discharging in a three-electrode Swagelok cell using a CHI 760 electrochemical

workstation (Fig. S9). Notably, zinc ions tend to occupy the nanocavities and migrate through the 3D tunnel of PBA frameworks at the equilibrium potential of Zn^{2+}/Zn conversion (Fig. S10). Next, we show some direct evidence to verify the feasibility of the above design strategy in regulating Zn deposition through oriented-attachment-initiated Zn (002) stacking on the lateral side of the PBA nanocubes. After electrodeposition, scanning electron microscopy (SEM) images show a highly oriented dense hexagonal Zn deposits on the PBA@Ti substrate with a smooth and flat surface, indicating preferred deposition of Zn (002) plane (Fig. 1d and Fig. S11). As illustrated in Fig. 1e and 1f, the HAADF/EDS analyses clearly show the adhesion of zinc on the surface of the NiFe-PBA cube after initial plating. To elucidate the role of PBA cubes in the initial Zn nucleation process, high-magnification TEM images of the PBA-Zn interface were used to characterize the lattice mismatch of PBA and adherent Zn (Fig. 1g and Fig. S12). Fig. 1g displays the low-lattice-mismatch interfaces between PBA and metallic Zn, ensuring atomically intimate and coherent contact between the two phases. The distance of squarely distributed metal nodes of PBA frameworks precisely matches twice the spacing of Zn (002) crystallographic facets, indicating that the design strategy of constructing a well-spaced ion tunnel matrix on the substrate is tenable.

Rational screening of an appropriate ion tunnel matrix

The above evidence preliminarily validates the regulatory effect of oriented-attached electrodeposition on the horizontal growth of Zn stacks. Notably, this strategy is in principle applicable not only to flat rigid substrates but also to flexible and woven substrates such as low-cost carbon cloth (CC). Next, we investigated the Zn plating and stripping performances

of CC decorated by different MOFs (MOF@CC) to determine suitable 'ion tunnel matrix' candidates. In this experiment, eight different MOF-decorated CC substrates, *i.e.*, ZnFe-PBA@CC, NiFe-PBA@CC, CuFe-PBA@CC, MnFe-PBA@CC, CeFe-PBA@CC, ZIF-8@CC and Zn-BTC@CC, were fabricated. These samples are all easily synthesized at scale and have reasonable chemical stability towards Zn deposition. As shown in Fig. S4, the scattered nanosized MOF particles are rooted on the CC and distributed uniformly. Generally, there are four types of ion trap structures for MOF inlays, i.e., cubic-type PBAs with face-centre-cubic (*fcc*) structure in space group Fm-3m (ZnFe-PBA, NiFe-PBA, CuFe-PBA), noncubic-type PBAs (MnFe-PBA, CeFe-PBA), cubic-type Zn-based MOF (Zn-BTC) and MOF with irregular or unequally spaced cage-type pores (ZIF-8). Before the CE evolution tests, the MOFs anchored on the fibre undergo zinc ion insertion via low-rate electrochemical discharging. Note that CE evolutions of various substrates were tested in 2.0 M $ZnSO_4$ electrolyte with a moderate and pragmatic current density of 0.5 mA cm^{-2}; this was advantageous for practical use. A rigorous 'reservoir-free' galvanostatic protocol with 100% ZUR at each cycle was applied for the initial screening experiment (Fig. S13). Substrates that pass the above protocol would have high capability to achieve high energy density Zn-based batteries.

Fig. 2a demonstrates that untreated CC substrate delivers a low and unstable CE evolution, indicating that the interwoven carbon fibre is insufficient to realize highly reversible Zn plating/stripping. The CC//Zn asymmetric cell shows a sharp decline in CE after only 26 cycles of plating/stripping, which is consistent with previous reports[10b, 17]. The

average CE and lifetime are enhanced significantly by inlaying cubic-type PBAs on CC substrates (Fig. 2b-d). The reversibility of Zn plating/stripping on the cubic-type PBA@CC substrates is much higher than those of their other counterparts. Furthermore, the ZnFe-PBA@CC sample shows a highly stable CE of 99.17% over 200 cycles (Fig. 2b), which is superior to other substrates. Similar impressive results were obtained for the other cubic-type MOF decorated substrate (Zn-BTC@CC), which favours a stable CE of 96.22% over 200 cycles (Fig. 2e). In contrast, the substrates decorated with monoclinic MnFe-PBA (Fig. S14) or hexagonal CeFe-PBA (Fig. 2f) deliver fluctuating CE and short lifespan, indicating severe parasitic reactions and dendrites. For the ZIF-8@CC sample, the plating/stripping efficiency rises slightly at first and then oscillates randomly, showing a sharp decline after 25 cycles (Fig. 2g). Fig. 2h summarizes the average CE of various MOF@CC substrates, and a definite trend is obtained. Both the average CE and lifetime of Zn plating/stripping can be remarkably improved via introducing cubic-type PBA on the CC substrate. However, once the chosen PBA is replaced by noncubic phase types, the effect on the enhancement of Zn plating/stripping reversibility is seriously reduced. An intriguing point is that Zn-BTC with cubic phase can also facilitate the highly reversible and stable Zn plating and stripping, although the effectiveness is not as pronounced as with cubic-type PBAs. If other types of MOFs (such as ZIF-8) are used as tunnel matrices, the reversibility becomes quite poor and almost identical to that of the untreated CC.

The above comparative tests show the relevance between the MOF structure and Zn plating/stripping reversibility (Fig. 2h). Cubic-type PBA has a *fcc* structure with an equally

spaced 3D ion trap matrix. From the crystal structure point of view, the cubic-type PBA is an excellent candidate for the ion tunnel matrix with fixed Zn^{2+} trapping sites because of its ~5 Å spaced cyanide-bridged architecture (Fig. S15). The Zn^{2+} trapped by the isometric ion trap functions as the initial source of metallic Zn nucleation, creating the Zn (002) preferential orientation because the distance between adjacent isometric cages of the cubic-type PBA framework is approximately twice the spacing of the Zn (002) crystal plane. This hypothesis can also rationalize the high average CE boosted by Zn-BTC as the spacing between the nanocavities in this cubic-type MOF is also approximately a multiple of the spacing of Zn (002) plane. The distinctly superior CE and horizontally distributed galvanized layer corroborate the optimization of the cubic phase PBA for substrates. Once the spacing of the ion tunnels is inappropriate and/or nonuniform in the vertical substrate direction, the reversibility of Zn plating/stripping deteriorates. Preliminary screening experiments show that the cubic phase PBA is very suitable as a zinc ion trap and tunnel matrix for optimizing the horizontally arranged and high reversibility of Zn anodes.

Electrochemical performance of the ZnFe-PBA@CC substrate

The Zn plating/stripping reversibility of ZnFe-PBA@CC substrates was investigated in low-cost 2.0 M $ZnSO_4$ electrolyte with a rigorous 'reservoir free' protocol in PBA@CC//Zn asymmetric cell with 100% ZUR of each cycle. In contrast to the unstable and rapid degradation of Zn plating/stripping on a bare CC, the CE of Zn plating/stripping on a ZnFe-PBA@CC substrate rapidly soars to 99 % in the first 10 cycles and stabilizes at 99.17% for 880 cycles at 0.5 mA cm^{-2} and 0.5 mAh cm^{-2} (Fig. 3a). As shown in Fig. 3b, the CE

evolution on ZnFe-PBA@CC was further investigated at a higher current density. Notably, the stable cycle is retained for more than 6000 cycles (1300 h) with an average CE of 99.48% at 100% ZUR at a higher current density of 5 mA cm^{-2}. The overpotential remains low (36.5 mV) and stable during plating/stripping cycles (Fig. S16-S17). Under practical protocol of 5 mA cm^{-2} and 2 mAh cm^{-2}, the ZnFe-PBA@CC substrate favours a long lifespan of 500 h and a superior average CE of 99.58% over 600 cycles (Fig. 3c). The asymmetric cell employing ZnFe-PBA@CC substrates deliver an average CE of 99.18% over 1900 cycles and manifested a high level of reversibility at high current density of 10 mA cm^{-2} (Fig. S18). The cell maintains steady operation over 1700 h in a conventional 2.0 M $ZnSO_4$ aqueous electrolyte without any modified additives. The long-term galvanostatic profiles in Fig. 3d, 3e further verify the high reversibility of the Zn plating/stripping on the ZnFe-PBA@CC substrate with 100% ZUR mode, as shown by the consistently small overpotential of ~21 mV over 1700 h.

Notably, the strategy of constructing PBA nanocubes is also efficient for flat rigid substrates, such as Ti foil (Fig. S19). The stability of the ZnFe-PBA@CC substrates were further tested in symmetric cell at a current density of 0.5 mA cm^{-2} with 25% ZUR (Fig. S20-S21). The stability of Zn-plated ZnFe-PBA@CC substrates greatly exceeds that of Zn-plated CC samples. The symmetric cells employing ZnFe-PBA@CC substrates manifested a high level of reversibility over a wide range of current densities. As an extreme check, we conducted plating/stripping tests of symmetric cells using different substrates with a ZUR of 83% at different current densities from 0.5 mA cm^{-2} to an unprecedented 50 mA

cm^{-2} (Fig. S22). A comparison between our Zn-plated PBA@CC anode and the reported Zn-limited studies[18] was summarized by considering the average CE according to the cumulative capacity of metal plating before shortening or overimpedance, which is a key metric of useful lifetime of Zn cell (Fig. 3f). The indicators presented in this work are comparable to or better than those of other reported Zn anodes at a ZUR of 100% each cycle.

Moreover, the PBA@CC substrate can be used in conjunction with other optimization strategies, such as electrolyte engineering, to further enhance the performance of a highly unitized Zn anode. As a demonstration of the co-optimization, we study the plating/stripping reversibility of Zn on PBA@CC in water-in-salt electrolytes (13.0 M $ZnCl_2$) that enables further suppressing side reactions. The Zn plating/stripping reaction was highly reversible at 0.5 mA cm^{-2} and 0.5 mAh cm^{-2}, as shown by the high CE of 99.0% for 500 cycles with 100% ZUR. The voltage profiles in Fig. S23-S24 confirm that the Zn plating/stripping was highly reversible over 2000 h of cycling (500 cycles), which contrasts with the sharply fluctuating CE and prompt cell degradation experienced on a CC.

Visualization of dendrite-free Zn plating process

To observe the modulating effect of PBA on horizontal deposition and dendrite suppression, the morphologies of the plated Zn layer on CC and PBA@CC substrates were examined. As illustrated in Fig. 4a-d, a significant nonuniform Zn deposition process can be observed on an unmodified CC substrate; randomly oriented plate-like Zn crystals formed at the nucleation stage. The observation that Zn tends to form anisotropic plate-like deposits is consistent with previous research on Zn anodes in aqueous $ZnSO_4$ electrolytes. After the

growth of the crystals (50th plating at 0.5 mA cm^{-2} and 2 mAh cm^{-2}), much thinner and sharper Zn plates with classical dendritic morphologies are observed on the CC surface (Fig. 4d). Some Zn plates are stacked vertically and easily flake off, producing an isolated "dead" Zn or even resulting in short-circuiting. In contrast, the initial Zn plating on the PBA@CC substrate begins in the vicinity of the PBA crystals (Fig. 4e-h), probably because the Zn ion trapped in the framework of PBA provides the initial nuclei for Zn deposition. Previous reports generally believed that a uniform Zn nuclei layer on the entire substrate is required to ensure dendrite-free horizontal growth during deposition. However, the nonuniform nucleation process of zinc on PBA@CC substrates does not affect the subsequent planar growth and dense deposition of Zn, providing a unique example against the classical design principle of horizontally arranged zinc anodes (Fig. 4g-h and Fig. S25). As Zn deposits to 2 mAh cm^{-2}, the nano crystals grow laterally and epitaxial growth along the carbon cloth surface to form a compact and uniform Zn layer. The PBA cubes remain stable and merge into the compact Zn layer. The horizontally arranged Zn deposition is highly homogeneous throughout a submillimetre region, as shown in Fig. S26, without any detectable indications of aggressive dendritic growth. A considerable portion of the Coulombic inefficiency of Zn plating/stripping comes from the isolated 'dead' Zn that only partially dissolve during subsequent cycles. As shown in Fig. S27, the PBA@CC substrate enables complete zinc dissociation after 50 cycles, with almost no residual zinc on the smooth CC fibre. In contrast, the CC substrate resides with 'dead' Zn that cannot be dissociated in the charged state, which comes from the accumulation of irreversible capacity during cycles. Notably, the ZnFe-PBA

nanocubes anchored on carbon cloth remain stable and basically keep their unique morphology even after 500th plating/stripping (Fig. S28).

In addition, Zn deposits intrinsically tend to form platelets and expose the closest packed (002) basal plane to minimize the surface free energy of hexagonal-close-packed (*hcp*) zinc crystals. The *hcp* Zn platelets deposited on CC and PBA@CC substrates behave distinct morphologies due to variations in the arrangement of the preferred crystallographic planes on the substrate. It has been reported that (101) and (100) are preferred crystal planes for host-less Zn deposition in aqueous $ZnSO_4$ electrolyte, which leads to the random distribution of Zn platelets (Fig. 4i). If the Zn (002) plane dominates, Zn plating prefer to be initiated in a horizontal direction, directing to sequentially growth of Zn platelets preferentially in a direction parallel to the substrate. TEM image (Fig. 4j) of Zn deposition on PBA@CC showed that a dense structure composed of platelets parallel to the substrate was obtained; this result with the SEM images indicated that horizontally arranged Zn was obtained by predominately modulating the (002) planes. The influence of the PBA on Zn deposition was analysed by using XRD measurements (Fig. 4k). For the Zn-deposited CC substrate, several peaks matching the pattern of the $Zn_4SO_4(OH)_6{\cdot}5H_2O$ byproduct and $ZnSO_4$ residual solute were observed, indicating the severe side reaction and the loose morphology of Zn deposition. Besides, a low $I_{(002)}/I_{(100)}$ of 1.33 was obtained, which was consistent with the haphazard stack of the Zn platelet shown by SEM images. In contrast, the Zn (002) plane located at $2\theta = 36.3°$ shows higher intensity for Zn deposited on PBA@CC. The high $I_{(002)}/I_{(100)}$ of 3.02 indicates the preferred deposition of Zn (002) plane. Similar preferred

deposition of (002) plane also proceeded on PBA@CC in 13.0 M $ZnCl_2$ electrolyte (Fig. S29).

Zinc migration mechanism during electrodeposition

In previous studies, there were two seemingly contradictory perceptions about whether metal ions (such as Zn^{2+}) inserted in the nanocavities of PBA could be pushed out (or dynamically replaced). Some studies have employed PBA as cathode material and concluded that metal ions can inserted into the nanocavities of PBA. These inserted charge carriers (such as Zn^{2+}) are considered to be lodged in the PBA framework and will not be pushed out unless the electrode undergo a high potential charging process[4b, 19]. In another category of studies, PBAs were used as a functional layer of battery separator or artificial SEI layer. Substantial evidence showed that metal ions can be dynamically replaced and pushed out from PBA framework even at low potential due to the large channels for ions shuttle[20]. In this work, we found that Zn^{2+} in the PBA nanocavities plays an important role for enhancing the plating/striping reversibility of PBA@CC substrate. To more thoroughly interrogate the nature of the Zn^{2+} in the PBA nanocavities, we studied its emigration and deposition behavior. In this section, we selected Zn^{2+}-inserted NiFe-PBA@CC as the target to focus on the Zn^{2+} in the nanocavities and avoid the interference of metal nodes.

The dynamic displacement of ions in nanocavities was confirmed by resolving XPS spectrum of Zn^{2+}-inserted NiFe-PBA sample that discharged in Na_2SO_4 electrolyte (see detail in Fig. S30-31). Next, an underpotential deposition (UPD) test was performed to clarify the depositional tendency of Zn^{2+} in PBA from a thermodynamic point of view. A zinc-inserted

NiFe-PBA@CC substrate was discharged at +0.05 V versus Zn^{2+}/Zn (denoted as UPD-PBA@CC) in 0.5 M Na_2SO_4 aqueous electrolyte to exclude the influence of zinc ions in the electrolyte and investigate the underpotential deposition behavior of Zn^{2+} in nanocavities. The Zn-plated PBA@CC (discharging at -0.1V versus Zn^{2+}/Zn in $ZnSO_4$ electrolyte), non-deposited PBA@CC and Zn foil sample were also tested for comparison. In the Fourier transform of k^2-weighted extended X-ray absorption fine structure (EXAFS) spectroscopy (Fig. 5a), the predominant peaks for three samples containing PBAs are almost identical in position, suggesting the nearly same coordination environment of Zn^{2+} in PBA framework and the stability of PBA during Zn plating. Notably, the peak appears at ~2.3 Å in UPD-PBA@CC (just as in Zn foil and Zn-plated PBA@CC) suggests the presence of Zn-metal, indicating that Zn^{2+} in nanocavities can migrate to the surface of PBA and contribute to underpotential deposition at a discharge potential higher than 0 V vs. Zn^{2+}/Zn. Wavelet transform-EXAFS (Fig. 5b-e) was also conducted to identify the Zn-Zn distance in UPD-PBA@CC sample. The presence of metallic Zn on UPD-PBA@CC suggests that Zn^{2+} in PBA framework possess a better tendency to be deposited compared with Zn^{2+} in the electrolyte from a thermodynamic point of view. That is, the Zn^{2+} inside PBA preferentially deposit in advance on the PBA surface to form a zinc layer which can regulate subsequent Zn deposition.

To further clarify the participation of Zn^{2+} in PBA for initial Zn plating, we studied the zinc migration mechanism in the electrodeposition process via the isotope tracking technique. Before Zn deposition, PBA@CC substrates undergo zinc ion insertion in a common $ZnSO_4$

electrolyte by using low-rate electrochemical discharging. Fig. S32 shows the EDS mapping of a NiFe-PBA nanocube after discharging. The uniform distributions of zinc in PBA cubes suggest the insertion of Zn^{2+} into PBA frameworks before Zn deposition. Fig. 5a shows the time-of-flight secondary ion mass spectrometry (TOF-SIMS) depth profiles of Zn in NiFe-PBA@CC before Zn deposition. There are four types of zinc isotopes in PBA frameworks, i.e., ^{64}Zn, ^{66}Zn, ^{67}Zn and ^{68}Zn. This can be rationalized by the fact that the abundances of these four isotopes in nature are 48.6%, 27.9%, 4.1%, and 18.8%, respectively. The depth profiles, combined with the 3D spatial configuration of the SIMS signal (inset of Fig. 5a), clearly demonstrate that the four zinc isotopes coexist from the surface to the interior of the PBA@CC substrate.

Next, the NiFe-PBA@CC substrate was transferred to a three-electrode Swagelok cell incorporated with $^{64}ZnSO_4$ aqueous electrolyte. The substrate was initially subjected to a single galvanostatic zinc deposition in a ^{64}Zn labelled electrolyte, followed by careful pickling to remove the zinc metal so that only the PBAs inlay on the carbon cloth remained. Based on the depth profiles and 3D visualization of the zinc isotope distribution in Fig. 5b, the proportion of ^{64}Zn in the PBA frameworks is much higher than that of the other isotopes of zinc. Specifically, the zinc ions trapped in the PBA nanocavities are replaced by $^{64}Zn^{2+}$ from the labelled $^{64}ZnSO_4$ electrolyte during electrodeposition. The above results indicate that the zinc ions in the tunnel matrix of PBA are continuously replaced by zinc ions in the electrolyte during deposition process. However, the deregulation of Zn^{2+} from the PBA nanocavities to the electrolyte is thermodynamically forbidden within the equilibrium

potential of Zn^{2+}/Zn conversion[21]. Combining the above evidence, the zinc migration and ion replacement mechanism during electrodeposition can be inferred, as schematically shown in Fig. 5c. The original zinc ions temporarily stored in the frameworks participated in the deposition reaction as the initial zinc source. PBA can be considered an ideal zinc ion tunnel matrix because its nanocavities are equally spaced at approximately 5 Å and exhibit a small lattice misfit with the (002) plane of metallic Zn. Thus, the trace amount of well-spaced zinc ions from the framework provides nuclei for Zn plating and locks the (002) crystallographic orientation. Additionally, Zn^{2+} in aqueous electrolyte could insert consecutively into the PBA framework at deposition potential to fill the vacant nanocavities created by outwards migration, ultimately leading to the continuous replacement of zinc ions inside the PBA. The above zinc isotope labelling studies highlight the critical function of zinc ions inside the isometric tunnel matrix and suggest a trapping-then-planting process during the initial deposition. Of note, if the PBA frameworks have not experiment zinc ions insertion before initial Zn deposition, the tunnel matrix loses its effect on the optimization of zinc anode reversibility (Fig. S33). This further indicates that PBA framework topology itself does not possess a crucial factor to guide zinc deposition. Instead, only when a large number of zinc ions are present inside the framework, the ion tunnel matrix can play the role of regulatory effect.

Full battery and pouch cell performance with a high ZUR

Due to the attractive Zn plating/stripping performance of the PBA@CC substrate, we carried out full cell investigations of the Zn-plated PBA@CC anode combined with the

polyaniline (PANI)-intercalated V_2O_5 (PVO) cathode[22]. The Zn//PVO full cell possesses a theoretical energy density of 228 Wh kg^{-1} in ideal case of 100% ZUR (based on the anode and cathode). The PVO of stacked nanosheets was synthesized through a hydrothermal reaction. Detailed structural characterization of the PVO cathode material are shown in Fig. S34. The low negative-to-positive capacity ratio (N/P) is a key parameter for evaluating Zn-based full cells with high energy density. N/P=1 in full cell operation is the ideal case, corresponding to the limiting cases where the ZUR is 100%. However, most research on Zn batteries has used a significant excess Zn reservoir (Zn foil or Zn sheet) to compensate for continuous anode consumption and maintain unsubstantial cycling stability. The excessive use of Zn causes the N/P to drastically increase to double or even triple digit numbers, which seriously declines the practical energy densities of the batteries and hinders their practical application.

Here, we assembled Zn-plated ZnFe-PBA@CC//PVO full cells using a 2.0 M $ZnSO_4$ aqueous electrolyte in a low N/P ratio of 1.2 and a high ZUR of 83%. As illustrated in Fig. 6a, the full cell with a N/P of 1.2 can be cycled stably for 360 cycles with a capacity retention of over 62% at a current density of 3 A g^{-1}. The cycling performance of the full cell with this high ZUR is comparable to that of a Zn foil//PVO configuration utilizing excess zinc with an N/P of approximately 20:1. In contrast, the Zn-plated CC//PVO full cell with an N/P of 1.2 delivers a low initial capacity and decays to approximately 7 mAh g^{-1} in only 50 cycles. ZUR is a key indicator for assessing the percentage of the theoretical energy density of aqueous Zn-based cells can be achieved at the device level. As illustrated in Fig. 6b and Fig. S35, the

Zn foil with low ZUR (less than 5%) presents at least 1800% overprovision of Zn anodes, resulting in the Zn foil//PVO pair with an imbalance mass configuration only being able to achieve 9% of the theoretical energy density. The PBA@CC architecture optimizes the N/P ratio and implements only a 20% Zn excess in battery construction, which achieves 91% of the promised energy density of the full cell by lowering the anode weight. The stark comparison of the galvanostatic charge/discharge curves of full cells using CC and PBA@CC substrates echoes the superior cycle performance of the Zn-plated PBA@CC//PVO battery at this high ZUR (Fig. 6c-d). The full cell using the PBA@CC substrate maintains similar charge/discharge curve profiles throughout 360 cycles, in sharp contrast to the Zn-plated CC//PVO cell, which displays increasingly steep discharge curves originating from Zn depletion after 10 cycles.

One of the most critical issues of existing studies on aqueous Zn batteries is that an excessive amount of Zn (such as a thick Zn plate) is applied to the anode, leading to a limited practical energy density. With a ZUR of less than 20%, the energy density of the Zn//PVO cell is even lower than those of commercial aqueous systems, such as lead-acid, Ni-Cd and Ni-MH batteries (Fig. 6e). Notably, the Zn//PVO full cell with a high ZUR of 83%, which in reliance on the highly reversible Zn plating/stripping of the PBA@CC substrate, exhibits a high energy density (214 Wh kg^{-1}) that overwhelms commercial aqueous batteries. As shown in Fig. 6f and Fig. S36, the Zn-plated PBA@CC//PVO full battery displays a superior and stable rate capability at various current densities of 0.1, 0.5, 1, 2, 3, 4 and 5 A g^{-1}, delivering reversible capacities of 398, 302, 269, 235, 212, 194 and 179 mAh g^{-1}, respectively. Finally,

an assessment of PBA@CC substrates was carried out by assembling an anode-limited 30×30 mm pouch cell (Fig. 6g and Fig. S37) consisting of Zn-plated PBA@CC//PVO, where the ZUR of the negative electrode was up to 83% (N/P=1.2). The inset in Fig. 6g vividly demonstrates the lightweight of the pouch cell with high ZUR: total mass of two anode-limited cells is lighter than one thick Zn sheet-based pouch cell. This anode-limited cell favours an initial energy density of 249 Wh kg^{-1} (based on anode and cathode) and maintains as much as 71% after 50 cycles at 0.5 A g^{-1}, demonstrating the superior Zn plating/stripping performance of the PBA@CC substrate and its potential for practical applications.

3. Conclusion

In summary, we demonstrated that cubic-type PBAs rooted on substrates can assist highly reversible Zn plating/stripping and achieve high ZURs for Zn anodes. In contrast to the previously reported PBA as host electrodes for various charge-carrier ions, our study focuses on exploiting the potential of its highly regular, equally spaced cubic topology features. The zinc ions trapped in the isometric nanocavities of PBA are well-spaced at approximately 5 Å and function as the initial source of metallic Zn nucleation, which initiate the oriented-attached Zn (002) preferential orientation and promote the lateral stacking of Zn nucleates. And this novel trapping-then-planting process is evidenced and revealed by our detailed spherical aberration electron microscope observation, Zn isotope tracking and TOF-SIMS technique, *etc*. The ZnFe-PBA@CC substrate has stable zinc plating/stripping for 6600 cycles (1320 h) at 5 mA cm^{-2} and delivers an average CE of 99.5% with a rigorous

100% ZUR protocol. The anode-limited Zn metal full cell demonstrates an energy density of 214 Wh kg^{-1} and retains ~62% of its capacity after 360 cycles under high ZUR (83%). This study successfully constructs a well-spaced ion tunnel matrix to modulate electrodeposition in a 3D view with microscopic or even atomic precision. We believe that this strategy can be in principal applied to other metal anodes and advance the commercial achievement of high energy densities for metal-based secondary batteries.

Supporting Information

Supporting Information is available from the Wiley Online Library or from the author.

Acknowledgements

This work was supported by the National Key Research and Development Program of China (No.2022YFB2404300, No.2020YFA0715000), National Natural Science Foundation of China (No.52101269, No.52127816, No.61905180, No.52072282), the China Postdoctoral Science Foundation (No.2021M692489), the Key R&D Program of Hubei Province (2022BAA028), State Key Laboratory of Advanced Technology for Materials Synthesis and Processing (WUT: 2022-KF-4) and Fundamental Research Funds for the Central Universities (WUT: 2182022333).

Conflict of Interest

The authors declare no conflict of interest.

Keywords

Aqueous zinc-ion battery, zinc metal anode, Prussian blue analogue, high zinc utilization rate, oriented attachment

Author contributions

L.M., D.D., K.F. and W.L. conceived the idea. D.D., W.L. and K.F. designed the experiment. D.D. performed the electrochemical tests and analyse the data. D.D. and K.F. participated in writing the paper. J.W. and R.Y. performed the characterizations of TEM analysis. K.F., J.Z., H.C. and X.Z. performed the conducted the local electrochemical measurements. D.D., K.F., W.L. and L.M. discussed the results. L.M. supervised the project. All authors have read and approved the final paper.

References

[1] a) C. Zhong, B. Liu, J. Ding, X. R. Liu, Y. W. Zhong, Y. Li, C. B. Sun, X. P. Han, Y. D. Deng, N. Q. Zhao, W. B. Hu, *Nat. Energy*. **2020**, *5*, 440; b) Y. F. Yuan, R. Sharpe, K. He, C. H. Li, M. T. Saray, T. C. Liu, W. T. Yao, M. Cheng, H. L. Jin, S. Wang, K. Amine, R. Shahbazian-Yassar, M. S. Islam, J. Lu, *Nat. Sustain.* **2022**, *5*, 890.

[2] X. L. Li, M. Li, Z. D. Huang, G. J. Liang, Z. Chen, Q. Yang, Q. Huang, C. Y. Zhi, *Energy Environ. Sci.* **2021**, *14*, 407.

[3] a) W. Sun, F. Wang, B. Zhang, M. Y. Zhang, V. Kupers, X. Ji, C. Theile, P. Bieker, K. Xu, C. S. Wang, M. Winter, *Science* **2021**, *371*, 46; b) L. S. Cao, D. Li, T. Pollard, T. Deng, B. Zhang, C. Y. Yang, L. Chen, J. Vatamanu, E. Y. Hu, M. J. Hourwitz, L. Ma, M. Ding, Q. Li, S. Y. Hou, K. Gaskell, J. T. Fourkas, X. Q. Yang, K. Xu, O. Borodin, C. S. Wang, *Nat. Nanotechnol.* **2021**, *16*, 902.

[4] a) Y. Shang, D. Kundu, *Joule* **2023**, *7*, 244; b) L. E. Blanc, D. Kundu, L. F. Nazar, *Joule* **2020**, *4*, 771; c) J. F. Parker, C. N. Chervin, I. R. Pala, M. Machler, M. F. Burz, J. W. Long, D. R. Rolison, *Science* **2017**, *356*, 415.

[5] L. Ma, M. A. Schroeder, O. Borodin, T. P. Pollard, M. S. Ding, C. Wang, K. Xu, *Nat. Energy* **2020**, *5*, 743.

[6] a) Z. Zhao, R. Wang, C. Peng, W. Chen, T. Wu, B. Hu, W. Weng, Y. Yao, J. Zeng, Z. Chen, P. Liu, Y. Liu, G. Li, J. Guo, H. Lu, Z. Guo, *Nat. Commun.* **2021**, *12*, 6606; b) M. Zhou, S. Guo, J. Li, X. Luo, Z. Liu, T. Zhang, X. Cao, M. Long, B. Lu, A. Pan, G. Fang, J. Zhou, S. Liang, *Adv. Mater.* **2021**, *33*, 2100187; c) F. W. Ming, Y. P. Zhu, G. Huang, A. H. Emwas, H. F. Liang, Y. Cui, H. N. Alshareef, *J. Am. Chem. Soc.* **2022**, *144*, 7160; d) M. Wang, J. Ma, Y. Meng, J. Sun, Y. Yuan, M. Chuai, N. Chen, Y. Xu, X. Zheng, Z. Li, W. Chen, *Angew. Chem. Int. Ed.* **2022**.

[7] a) J. Cao, D. Zhang, C. Gu, X. Wang, S. Wang, X. Zhang, J. Qin, Z.-S. Wu, *Adv. Energy Mater.* **2021**, *11*, 2101299; b) J. X. Zheng, L. A. Archer, *Sci. Adv.* **2021**, *7*; c) Y. Zou, X. Yang, L. Shen, Y. Su, Z. Chen, X. Gao, J. Zhou, J. Sun, *Energy Environ. Sci.* **2022**, *15*, 5017.

[8] a) C. Li, A. Shyamsunder, A. G. Hoane, D. M. Long, C. Y. Kwok, P. G. Kotula, K. R. Zavadil, A. A. Gewirth, L. F. Nazar, *Joule* **2022**, *6*, 1103; b) L. Cao, D. Li, T. Pollard, T. Deng, B. Zhang, C. Yang, L. Chen, J. Vatamanu, E. Hu, M. J. Hourwitz, L. Ma, M. Ding, Q. Li, S. Hou, K. Gaskell, J. T. Fourkas, X. Q. Yang, K. Xu, O. Borodin, C. Wang, *Nat. Nanotechnol*. **2021**, *16*, 902; c) Z. K. Guo, L. S. Fan, C. Y. Zhao, A. S. Chen, N. N. Liu, Y. Zhang, N. Q. Zhang, *Adv. Mater.* **2022**, *34*.

[9] a) X. Zhang, J. Li, K. Qi, Y. Yang, D. Liu, T. Wang, S. Liang, B. Lu, Y. Zhu, J. Zhou, *Adv. Mater.* **2022**, *34*, 2205175; b) Y. Zhang, X. Li, L. S. Fan, Y. Shuai, N. Q. Zhang, *Cell Rep. Phys. Sci.* **2022**, *3*.

[10] a) Z. Wang, H. Chen, H. Wang, W. Huang, H. Li, F. Pan, *ACS Energy Lett.* **2022**, 4168; b) J. Zheng, D. C. Bock, T. Tang, Q. Zhao, J. Yin, K. R. Tallman, G. Wheeler, X. Liu, Y. Deng, S. Jin, A. C. Marschilok, E. S. Takeuchi, K. J. Takeuchi, L. A. Archer, *Nat. Energy* **2021**, *6*, 398; c) X. Z. Yang, C. Li, Z. T. Sun, S. Yang, Z. X. Shi, R. Huang, B. Z. Liu, S. Li, Y. H. Wu, M. L. Wang, Y. W. Su, S. X. Dou, J. Y. Sun, *Adv. Mater.* **2021**, *33*; d) L. Y. Wang, W. W. Huang, W. B. Guo, Z. H. Guo, C. Y. Chang, L. Gao, X. Pu, *Adv. Funct. Mater.* **2022**, *32*, 2108533; e) A. S. Chen, C. Y. Zhao, J. Z. Gao, Z. K. Guo, X. Y. Lu, J. C. Zhang, Z. P. Liu, M. Wang, N. N. Liu, L. S. Fan, Y. Zhang, N. Q. Zhang, *Energy Environ. Sci.* **2023**, *16*, 275.

[11] J. Zheng, Q. Zhao, T. Tang, J. Yin, C. D. Quilty, G. D. Renderos, X. Liu, Y. Deng, L. Wang, D. C. Bock, C. Jaye, D. Zhang, E. S. Takeuchi, K. J. Takeuchi, A. C. Marschilok, L. A. Archer, *Science* **2019**, *366*, 645.

[12] Y. P. Zhu, Y. Cui, H. N. Alshareef, *Nano Lett.* **2021**, *21*, 1446.

[13] Z. Wang, J. H. Huang, Z. W. Guo, X. L. Dong, Y. Liu, Y. G. Wang, Y. Y. Xia, *Joule* **2019**, *3*, 1289.

[14] X. Li, Q. Li, Y. Hou, Q. Yang, Z. Chen, Z. Huang, G. Liang, Y. Zhao, L. Ma, M. Li, Q. Huang, C. Zhi, *ACS Nano* **2021**, *15*, 14631.

[15] X. Zheng, Z. Liu, J. Sun, R. Luo, K. Xu, M. Si, J. Kang, Y. Yuan, S. Liu, T. Ahmad, T. Jiang, N. Chen, M. Wang, Y. Xu, M. Chuai, Z. Zhu, Q. Peng, Y. Meng, K. Zhang, W. Wang, W. Chen, *Nat. Commun.* **2023**, *14*, 76.

[16] a) K. Fu, J. Chen, R. Xiao, J. Zheng, W. H. Tian, X. G. Li, *Energy Environ. Sci.* **2018**, *11*, 1563; b) W. Chen, Y. Jin, J. Zhao, N. Liu, Y. Cui, *Proc. Natl. Acad. Sci. U.S.A.* **2018**, *115*, 11694.

[17] Q. H. Cao, H. Gao, Y. Gao, J. Yang, C. Li, J. Pu, J. J. Du, J. Y. Yang, D. M. Cai, Z. H. Pan, C. Guan, W. Huang, *Adv. Funct. Mater.* **2021**.

[18] a) W. C. Du, S. Huang, Y. F. Zhang, M. H. Ye, C. C. Li, *Energy Storage Mater.* **2022**, *45*, 465; b) N. Hu, H. Y. Qin, X. Y. Chen, Y. P. Huang, J. Xu, H. B. He, *Front. Chem.* **2022**, *10*; c) W. B. Li, Q. Zhang, Z. F. Yang, H. M. Ji, T. Q. Wu, H. Wang, Z. W. Cai, C. L. Xie, Y. X. Li, H. Y. Wang, *Small* **2022**, *18*; d) Z. D. Zhao, R. Wang, C. X. Peng, W. J. Chen, T. Q. Wu, B. Hu, W. J. Weng, Y. Yao, J. X. Zeng, Z. H. Chen, P. Y. Liu, Y. C. Liu, G. S. Li, J. Guo, H. B. Lu, Z. P. Guo, *Nat. Commun.* **2021**, *12*; e) H. Chen, W. J. Zhou, M. F. Chen, Q. H. Tian, X. Han, J. Z. Chen, *Nano Res.*; f) D. D. Wang, D. Lv, H. X. Liu, S. J. Zhang, C. Wang, C. T. Wang, J. Yang, Y. T. Qian, *Angew. Chem.-Int. Edit.* **2022**, *61*; g) D.

Xie, Z. W. Wang, Z. Y. Gu, W. Y. Diao, F. Y. Tao, C. Liu, H. Z. Sun, X. L. Wu, J. W. Wang, J. P. Zhang, *Adv. Funct. Mater.* **2022**, *32*; h) X. T. Zhang, J. X. Li, D. Y. Liu, M. K. Liu, T. S. Zhou, K. W. Qi, L. Shi, Y. C. Zhu, Y. T. Qian, *Energy Environ. Sci.* **2021**, *14*, 3120; i) M. L. Wang, X. Y. Wu, D. Yang, H. A. Zhao, L. He, J. R. Su, X. Zhang, X. X. Yin, K. N. Zhao, Y. Z. Wang, Y. J. Wei, *Chem. Eng. J.* **2023**, *451*; j) W. Ling, Q. X. Yang, F. N. Mo, H. Lei, J. Q. Wang, Y. Jiao, Y. J. Qiu, T. Chen, Y. Huang, *Energy Storage Mater.* **2022**, *51*, 453; k) R. F. Xue, J. Y. Kong, Y. Wu, Y. Y. Wang, X. Y. Kong, M. Gong, L. Zhang, X. Lin, D. R. Wang, *J. Mater. Chem. A*. **2022**, *10*, 10043; l) J. Q. Zhou, L. F. Zhang, M. J. Peng, X. Zhou, Y. F. Cao, J. Liu, X. W. Shen, C. L. Yan, T. Qian, *Adv. Mater.* **2022**, *34*.

[19]a) L. Y. Zhang, L. Chen, X. F. Zhou, Z. P. Liu, *Adv. Energy Mater.* **2015**, *5*; b) M. Huang, J. S. Meng, Z. J. Huang, X. P. Wang, L. Q. Mai, *J. Mater. Chem. A*. **2020**, *8*, 6631.

[20]a) Y. Liu, Y. X. Li, X. M. Huang, H. Cao, Q. J. Zheng, Y. Huo, J. X. Zhao, D. M. Lin, B. G. Xu, *Small* **2022**, *18*; b) M. C. Du, Z. H. Peng, X. Long, Z. J. Huang, Z. W. Lin, J. H. Yang, K. Ding, L. Y. Chen, X. J. Hong, Y. P. Cai, Q. F. Zheng, *Nano Lett.* **2022**, *22*, 4861; c) G. Y. Jiang, K. Y. Li, J. Y. Mao, N. Jiang, J. P. Luo, G. Y. Ding, Y. H. Li, F. G. Sun, B. Dai, Y. S. Li, *Chem. Eng. J.* **2020**, *385*.

[21] a) L. Zhang, L. Chen, X. Zhou, Z. Liu, *Sci Rep*. **2015**, *5*, 18263; b) L. Y. Zhang, L. Chen, X. F. Zhou, Z. P. Liu, *Adv. Energy Mater.* **2015**, *5*, 1400930.

[22] a) C. H. Han, J. Zhu, K. Fu, D. Deng, W. Luo, L. Q. Mai, *ChemComm.* **2022**, *58*, 791; b) S. Liu, H. Zhu, B. Zhang, G. Li, H. Zhu, Y. Ren, H. Geng, Y. Yang, Q. Liu, C. C. Li, *Adv. Mater.* **2020**, *32*, 2001113.

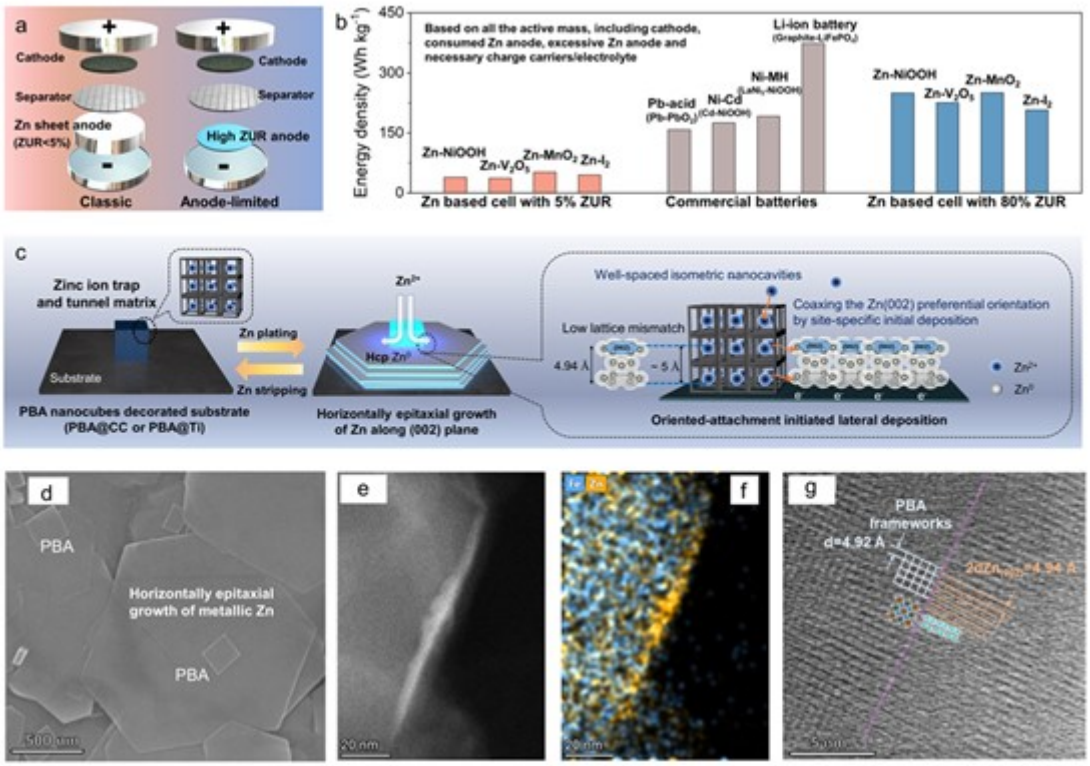

Fig. 1 Significance of high ZUR for zinc metal batteries and oriented attachment mechanism for lateral stacking of Zn. (a) Schematic illustrations of two different Zn metal battery configurations, i.e., classic battery with a thick Zn sheet anode (left) and anode-limited battery with high ZUR (right). (b) Comparison of the theoretical energy densities of different batteries based on all the active mass. (c) Schematic illustration of the lateral stacking on a well-spaced zinc ion tunnel matrix and the oriented attachment mechanism for site-specific initial nucleation. (d) SEM image of Zn-plated PBA@Ti substrate. (e, f) TEM image (e) and EDS analysis (f) of the Zn-plated NiFe-PBA cube. (g) High-magnification TEM image of the PBA-Zn heterointerface.

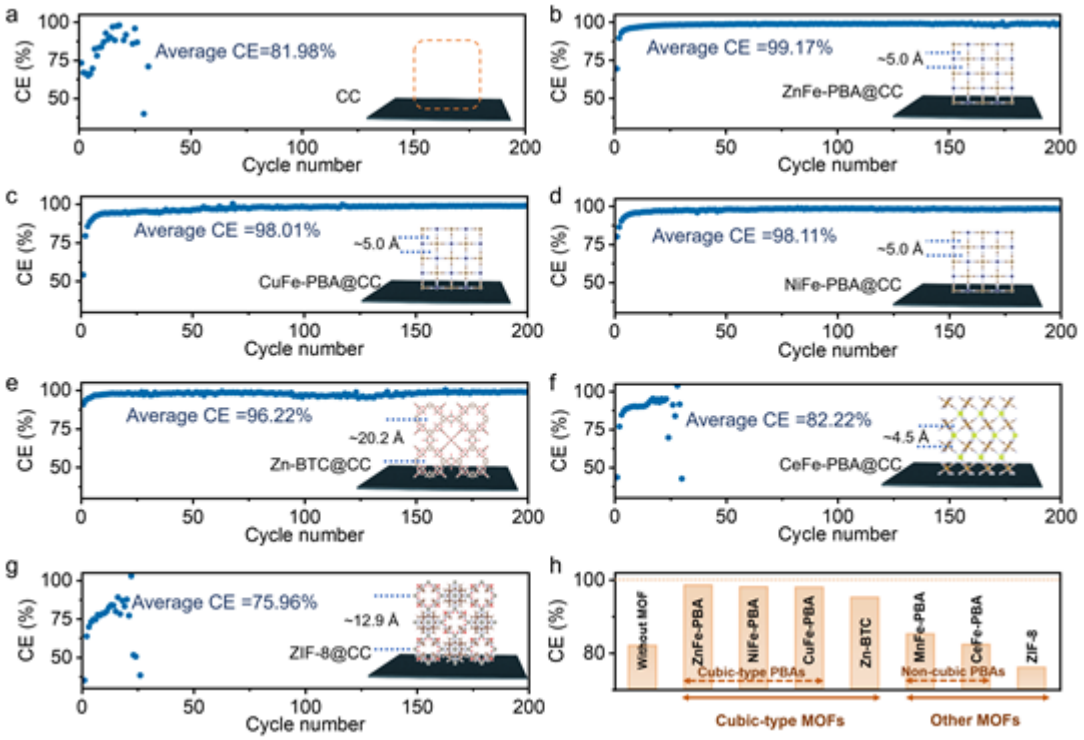

Fig. 2 Rational screening of several typical metal-organic frameworks. (a-g) CE evolution on cycling asymmetric cells at 0.5 mA cm^{-2} with a capacity of 0.5 mAh cm^{-2} using substrates of (a) CC, (b) ZnFe-PBA, (c) CuFe-PBA@CC, (d) NiFe-PBA@CC, (e) Zn-BTC@CC and (f) CeFe-PBA@CC. (g) ZIF-8@CC. (h) Illustration of the rational screening of MOFs for highly reversible Zn plating/stripping.

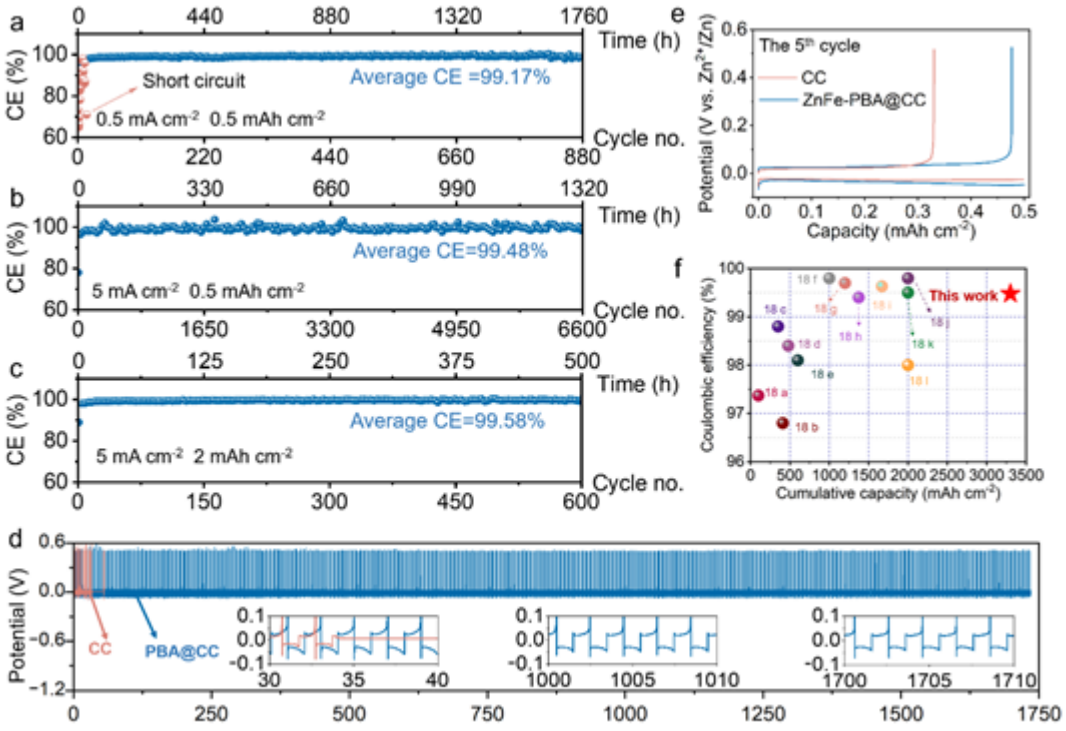

Fig. 3 Electrochemistry studies of Zn plating/stripping reversibility of the ZnFe-PBA@CC substrate. (a-c) CE evolution on cycling asymmetric cells under different conditions: (a) 0.5 mA cm^{-2} and 0.5 mAh cm^{-2}, (b) 5.0 mA cm^{-2} and 0.5 mAh cm^{-2} and (c) 5.0 mA cm^{-2} and 2.0 mAh cm^{-2}. (d) Long-term galvanostatic cycling of the ZnFe-PBA@CC//Zn and CC//Zn asymmetrical cells at 0.5 mA cm^{-2} with a capacity of 0.5 mAh cm^{-2}. Inset: The detailed voltage profiles of the cells at different stages. (e) Voltage profile comparison of the CC and ZnFe-PBA@CC electrodes at 0.5 mA cm^{-2} and 0.5 mAh cm^{-2} in the 5th cycle. (f) Comparison between the Zn plating/stripping performance of the asymmetric cells in this study and those reported based on two key parameters: CE and cumulative capacity.

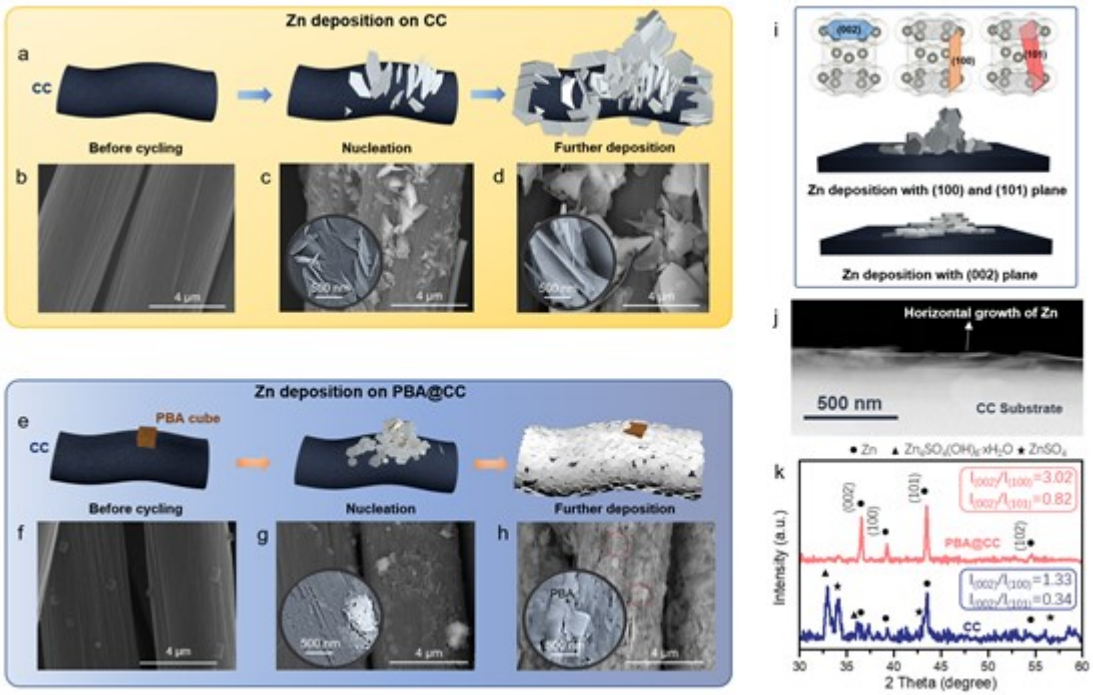

Fig. 4 Morphologies of plated Zn on different substrates. (a) Schematic diagrams of the morphology evolution of Zn electrodeposition on the CC substrate. (b-d) SEM images of Zn deposits on CC with a current density of 0.5 mA cm^{-2} at different deposition capacities of (b) 0 mAh cm^{-2}, (c) 0.1 mAh cm^{-2} and (d) 2 mAh cm^{-2}. Insets: Magnified images of aggravated dendrite formation. (e) Schematic diagrams of the morphology evolution of Zn electrodeposition on the ZnFe-PBA@CC substrate. (f-h) SEM images of Zn deposits on ZnFe-PBA@CC with a current density of 0.5 mA cm^{-2} at different deposition capacities of (f) 0 mAh cm^{-2}, (g) 0.1 mAh cm^{-2} and (h) 2 mAh cm^{-2}. Insets: Magnified images of the Zn deposits in the vicinity of the PBA nanocube. (i) Schematic illustration of the effect of the preferred orientation crystal on Zn deposition. (j) TEM image of the cross-sectional view of the Zn-plated ZnFe-PBA@CC substrate. (k) XRD results for the Zn deposits on CC and ZnFe-PBA@CC substrates.

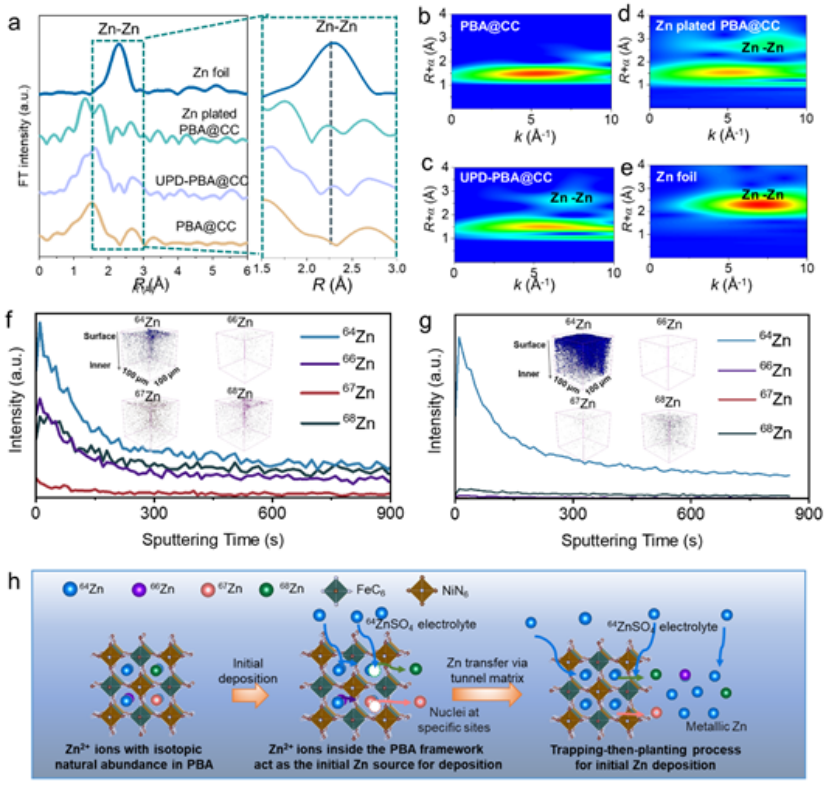

Fig. 5 Underpotential deposition and zinc migration mechanism. (a) Fourier transformation (FT)-EXAFS spectra of Zn element of UPD-PBA@CC and other contrast samples. (b-e) Wavelet transform (WT)-EXAFS of k^2-weighted k-space spectra of Zn for (b) PBA@CC, (c) UPD-PBA@CC, (d) Zn-plated PBA@CC and (e) Zn foil. (f) TOF-SIMS depth profiles of the four zinc isotopes collected from the NiFePBA@CC substrate with preinserted zinc ions in the common $ZnSO_4$ solution. Inset: The constructed 3D configuration of the four zinc isotopes. (g) TOF-SIMS depth profiles of the four zinc isotopes collected from the NiFe-PBA@CC substrate that underwent Zn deposition and pickling in $^{64}ZnSO_4$ electrolyte. (h) Schematic illustration of the zinc migration mechanism during electrodeposition.

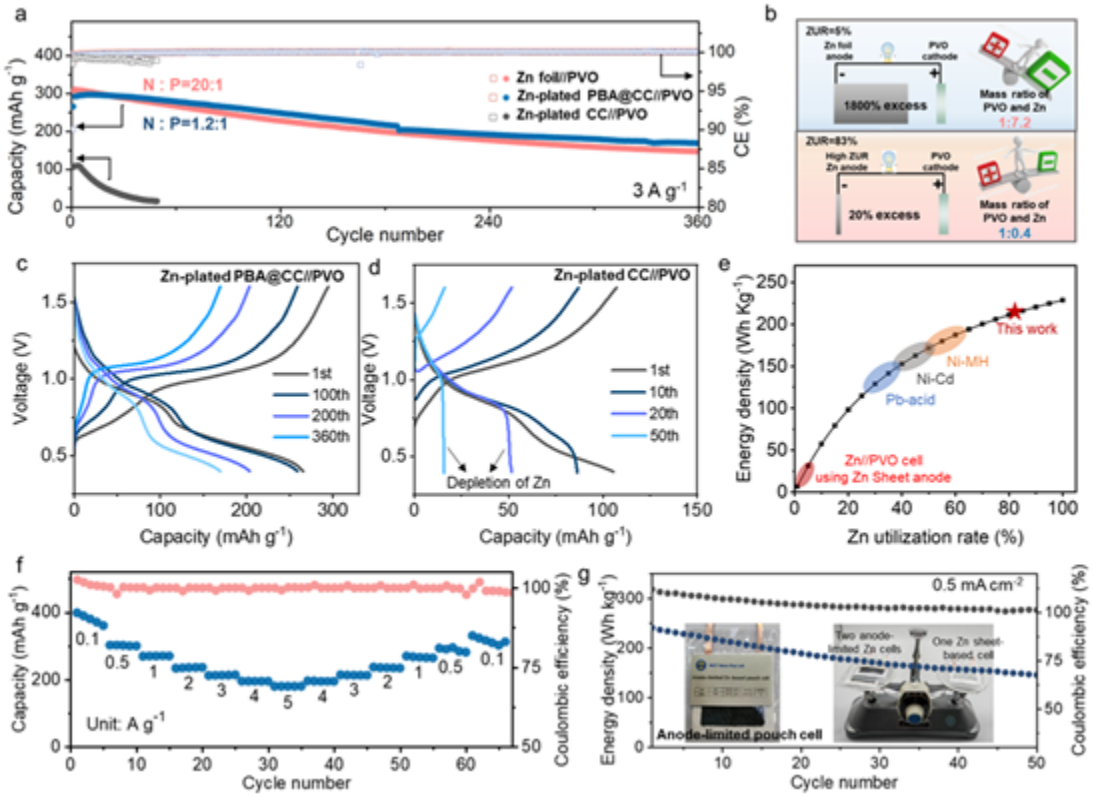

Fig. 6 Electrochemical performance of full cells with a high ZUR. (a) Cycle performances of full cells using different anodes. The Zn-plated PBA@CC//PVO full cell was tested at an N/P of 1.2, i.e., 83% ZUR. (b) Configuration of the anode and utilization ratio of the theoretical energy density of the classic Zn sheet-based battery and anode-limited Zn battery with 83% ZUR. (c, d) Galvanostatic voltage profiles of full cells with the configuration of (c) Zn-plated PBA@CC//PVO and (d) Zn-plated CC//PVO. (e) The calculated specific energy of a Zn//PVO battery as a function of increasing ZUR based on all the active mass. The shaded areas highlight the ranges of energy density of different aqueous battery systems. (f) Rate capability and corresponding CE of the Zn-plated PBA@CC//PVO coin cell at current densities ranging from 0.1 to 5 A g^{-1}. (g) Specific energy density evolution of the anode-limited pouch cells at 0.5 mA cm^{-2}. Inset: Exhibition of the pouch cell and its light weight advantage.

WILEY-VCH

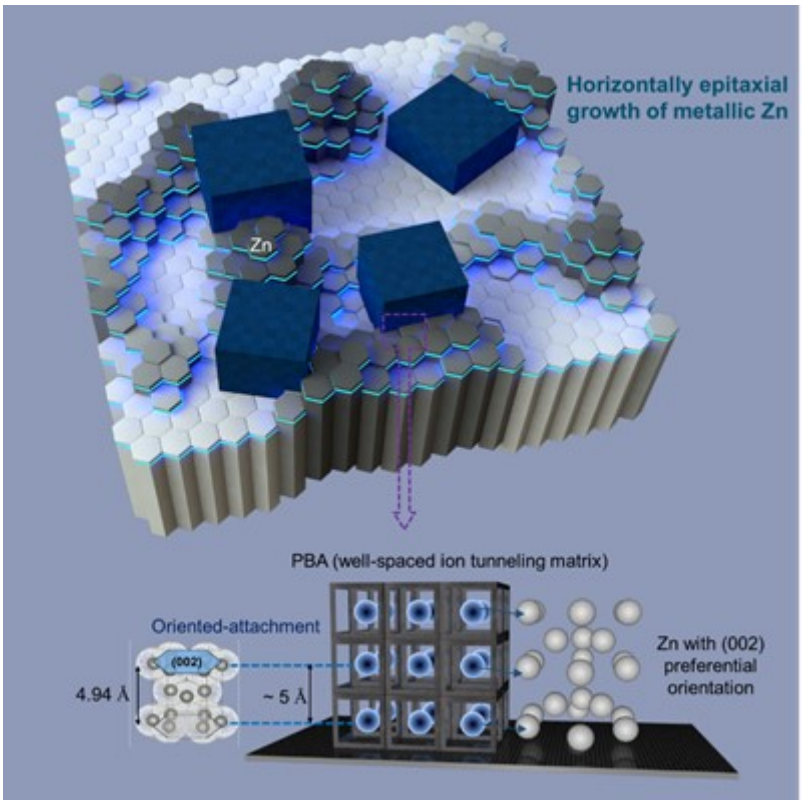

A strategy of “trapping-then-planting” oriented-attached deposition is demonstrated towards high performance zinc metal anode battery. Stable zinc plating/stripping for 6600 cycles (1320 h) at 5 mA cm^{-2} and a Coulombic efficiency of 99.5% with a rigorous 100% ZUR (zinc utilization ratio) protocol are realized. Moreover, an anode-limited pouch cell with a low N/P of 1.2 that displays an energy density of 279 Wh kg^{-1} is constructed; this greatly exceeds commercial aqueous batteries.